CHEMISTRY

# Anisotropic nanocrystal shape and ligand design for co-assembly

**Katherine C. Elbert[1†], William Zygmunt[2†], Thi Vo[2†], Corbin M. Vara[3], Daniel J. Rosen[3], Nadia M. Krook[3‡], Sharon C. Glotzer[2,4,5]*, Christopher B. Murray[1,3]***



**The use of nanocrystal (NC) building blocks to create metamaterials is a powerful approach to access emergent materials. Given the immense library of materials choices, progress in this area for anisotropic NCs is limited by the lack of co-assembly design principles. Here, we use a rational design approach to guide the co-assembly of two such anisotropic systems. We modulate the removal of geometrical incompatibilities between NCs by tuning the ligand shell, taking advantage of the lock-and-key motifs between emergent shapes of the ligand coating to subvert phase separation. Using a combination of theory, simulation, and experiments, we use our strategy to achieve co-assembly of a binary system of cubes and triangular plates and a secondary system involving two two-dimensional (2D) nanoplates. This theory-guided approach to NC assembly has the potential to direct materials choices for targeted binary co-assembly.**

## INTRODUCTION

Advances in synthetic capabilities have opened up access to an extensive library of experimentally realizable anisotropic nanocrystal (NC) building blocks (*1*–*5*), directing attention toward their usage in self-assembly for a wide range of exciting, emergent morphologies (*6*–*12*). These anisotropic NCs are of particular interest, as NC architecture and orientation within thin films are critical to optimize materials properties (*13*–*15*). However, systems of anisotropic NCs can experience many kinetic barriers along the path toward forming their thermodynamic equilibrium structures (*16*), resulting from NCs having to balance their spatial and orientational distributions. As such, experimental realizations of anisotropic NC self-assembly are more challenging and less common relative to their spherical counterparts. Counter to binary spherical systems, there exists no robust/predictive models for predicting ligand-mediated self-assembly, compounding difficulties in their rational design and co-assembly (*17*). This is especially true for the co-assembly of two differently shaped NCs. Unlike the large library of accessible lattices for binary spherical systems (*18*–*20*), previous examples of co-assembly of anisotropic building blocks are those designed to take advantage of shape complementarity and stoichiometries in driving cocrystallization (*21*–*24*). Having design rules for co-assembly of specific NC choices is critical, as this would unlock access to metamaterials with emergent properties (*25*–*31*). The ability to dope controlled ratios of NCs into a film of dissimilar NCs without disrupting the matrix structure would allow for a spectrum of stoichiometries to be realized (*32*, *33*), providing an additional knob to tune the metamaterial's properties.

Recent works have shown that the morphology of the ligand shell coating the NCs can modulate the effective shape of the composite building block (*34*). Rather than explicitly using a concave NC core, we instead use a theory-driven approach to select for two pairs of ligand-convex NC combinations that produce the emergent shape complementarity of interest. Given the large phase space of experimental handles across both NC shape and ligand architecture, we limit our NCs to a thin-film, binary system of two-dimensional (2D) triangular plates and 3D cubes, PbTe and $LaF_3$, respectively. $LaF_3$ is a dielectric material that is monodisperse in shape and size (*35*), and PbTe cubes exhibit tunable optical and semiconducting properties (*36*–*38*). Given that these two materials are known to phase segregate within films, there exists a chemical impetus working against co-assembly.

Here, we provide a joint study (theory, simulation, and experimental) for our design strategy, illustrated in Fig. 1. We theoretically optimize across three experimental handles—ligand types, plate to cube stoichiometric ratio, and annealing temperature—and select for the composite set of parameters that counterbalance against the segregation. Theoretical predictions are then quickly validated using Monte Carlo simulations, and we then show that experimental realization of our choice of design parameters produce the targeted self-assembled morphologies. Last, we extend our design principles of co-assembly to a system of two 2D NCs: $LaF_3$ triangular plates and $GdF_3$ rhombic plates.

## RESULTS

### Theory-guided design

To understand the driving forces underlying the conditions required to drive co-assembly of cubes and triangular plates, we construct a phase diagram of relevant morphologies using a thermodynamic perturbation theory (TPT) (see Methods) (*39*, *40*). Using TPT, we can compute the lattice free energy of formation, $\Delta G$, for competing structures of the cube/plate system and construct a phase diagram across the thermodynamic handles of stoichiometry and interaction strength. TPT necessitates a potential mean force (PMF) for cube-cube (CC), plate-plate (PP), and cube-plate (CP) interactions. Computing PMFs requires a selection of the ligand type grafted onto each particle. Previous experimental works have shown that oleic acid (OA) is effective at mediating colloidal assembly and provides a good starting point. Computing the PMFs and subsequent $\Delta G$ for

[1]Department of Chemistry, University of Pennsylvania, Philadelphia, PA 19104, USA. [2]Department of Chemical Engineering, University of Michigan, Ann Arbor, MI 48109, USA. [3]Department of Materials Science and Engineering, University of Pennsylvania, Philadelphia, PA 19104, USA. [4]Department of Materials Science and Engineering, University of Michigan, Ann Arbor, MI 48109, USA. [5]Biointerfaces Institute, University of Michigan, Ann Arbor, MI 48109, USA.
*Corresponding author. Email: cbmurray@sas.upenn.edu (C.B.M.); sglotzer@umich.edu (S.C.G.)
†These authors contributed equally to this work.
‡Present address: DuPont Co., Wilmington, DE 19803, USA.

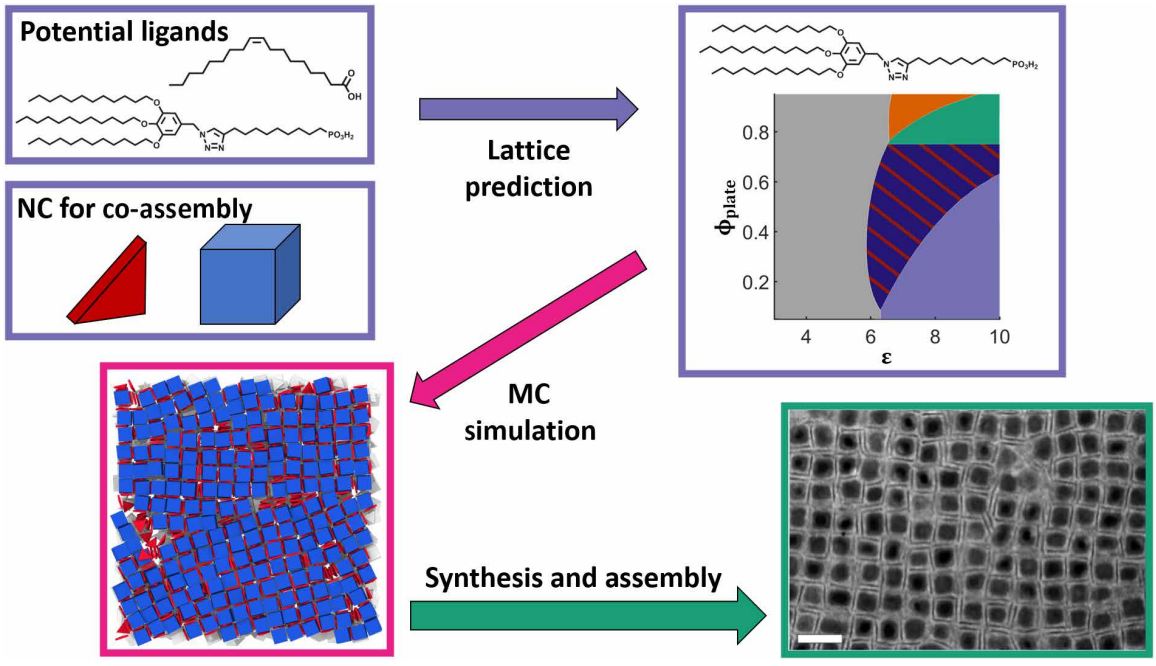


**Fig. 1. Schematic of design workflow.** Illustration of design strategy, demonstrating how lattice prediction methods (purple) lead to a feasible set of parameters for co-assembly, which are verified by computation (pink) and then realized experimentally (green). (Top left quadrant) Nanocrystals and ligands tested in the theoretical screening, serving as input to TPT. (Top right quadrant) Representative phase diagram for system computed from using TPT. (Bottom left quadrant) Phase diagram guides selection of phase space for Monte Carlo simulation. (Bottom left quadrant) Experimental realization of the designed system from both theory and MC validation. Scale bar in TEM image, 50 nm.

competing structures with OA as the ligand yields the phase diagram shown in Fig. 2A, revealing a region where co-assembly is thermodynamically preferred. However, this co-assembly regime is small compared to those of its competing structures, presenting challenges for experimental realization due to anticipated kinetic traps. As an alternative, we turn to using dendrimeric ligands (as opposed of OA) that have been shown to enhance both yield and stability of colloidal crystals (*34*, *41*). For simplicity, we chose the polycatenar ligand (PCL), a generation zero dendrimer. Using scaling arguments from our previous works (*34*), we determine PCL distributions on the surfaces of cubes and triangular plates and compute respective CC, PP, and CP PMFs. The updated phase diagram now yields the result shown in Fig. 2B. Here, we note that TPT calculations are for a theoretically perfect unit cell, where plates are sandwiched between cubes as that was the targeted co-assembly structure. As such, we only consider the parallel to film plate alignment in the phase-separated morphology (orange) in the construction of our phase diagram.

Direct comparison between Fig. 2 (A and B) reveals a growth in the co-assembly region (dark blue) along both the inverse temperature (ε) and stoichiometry axis. To understand the driving force behind enhanced co-assembly, we overlay the individual radial distribution functions, $g(r)$, for the co-assembled lattice of interest with their respective PMF for both OA and PCL to highlight differences between predicted interactions (Fig. 3, B to D).

Before comparing differences between PMFs for OA versus PCL, it is instructive to note features that emerge from the PMFs. First, PMFs show the strongest net attraction for CP interactions, irrespective of ligand. Naively, one would expect that CP and PP interactions are on par with each other as both should be dominated by the larger facet on the triangular plate. However, for CP interactions, the plate's

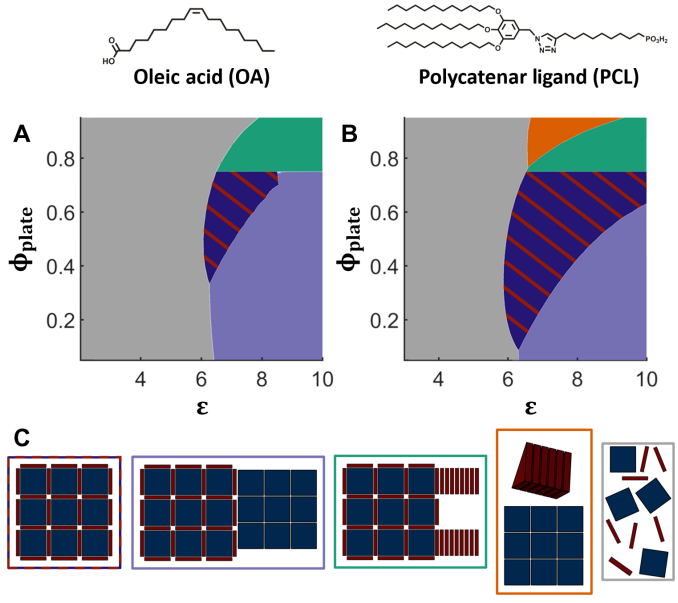


**Fig. 2. Theoretical prediction of co-assembly phase space.** Phase diagram for cube and triangular plate co-assembly for (**A**) OA ligand and (**B**) PCL, with ligand structures shown above. (**C**) Representative snapshots of the crystal structures used in construction of the phase diagrams. Border coloring corresponds to each respective phase.

face takes up ~43% of the cube's face, leaving excess ligands to interact with those occupying the edges of the plates. This additional face-edge contact favors CP over PP alignment, driving co-assembly. Within the co-assembled lattice, all PP contact distances—peaks in

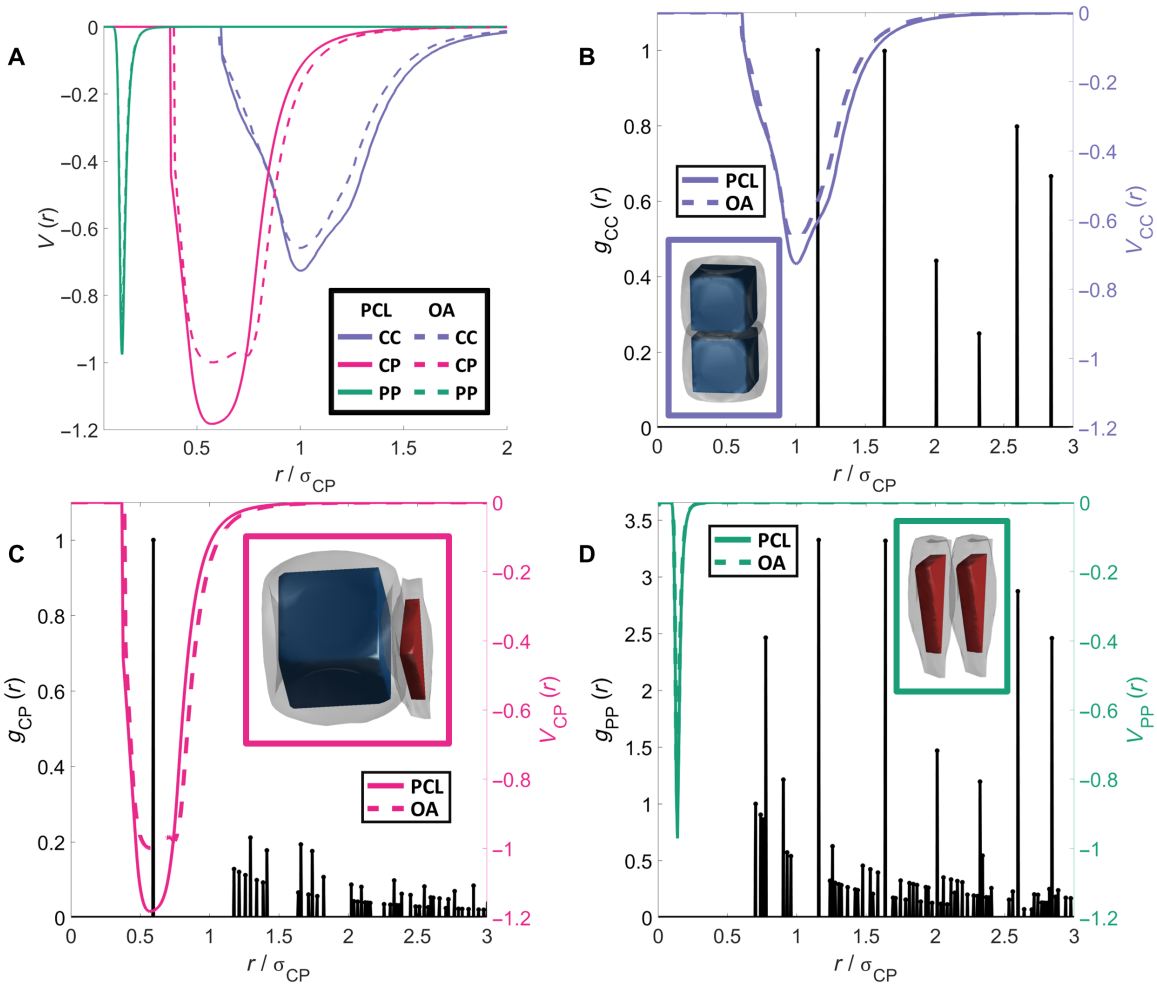


**Fig. 3. Differences in interparticle interactions for different ligands drive enhanced co-assembly.** (**A**) Computed PMF for CC, PP, and CP interactions. (**B**) Radial distribution function (black lines show peak locations) for CC, $g_{CC}(r)$, overlaid with PMF for CC. (**C**) Radial distribution function for CP, $g_{CP}(r)$, overlaid with PMF for CP. (**D**) Radial distribution function for PP, $g_{PP}(r)$, overlaid with PMF for PP. All PMFs shown are for relative orientation between NCs shown in the inset for (B) to (D). For all panels, dashed lines indicate PMF for OA and solid line is PMF for PCL.

$g_{PP}(r)$—fall well outside the interaction range defined by the PP's PMF (Fig. 3D). Conversely, the first peak in $g_{CC}(r)$ falls inside the range of the computed PMF for CC (Fig. 3B). These features suggest that CC interactions further stabilize the co-assembled lattice, while PP contacts do not. In short, introducing cubes into systems of triangular plates serves as a handle to tune co-assembly. Because of strong CP face-face interactions, cubes induce a preference for face-face contacts between cubes and plates. With increasing cube concentrations, CC interactions pull other cubes into the growing structure, enhancing existing CP interactions by locking plates in place between cubes while simultaneously gaining additional stabilizing CC contacts.

We now discuss enhancement in the co-assembly region upon transition from OA to PCL. PMFs shown in Fig. 3A indicate that CP interaction well is substantially deeper for the PCL than for OA, whereas CC and PP are relatively the same. As discussed above, CP interactions prevent phase separation and provides the dominant interaction driving lattice stability. The lower CP potential well increases the lattice's free energy of formation, thereby broadening the co-assembly regime. The origin of this deeper well can be understood through visualization of the ligand corona about each NC (insets; Fig. 3, B to D). Switching to the PCL produces a dimple in the corona at the faces of each cube. This dimple enables the plates to sit closer to the cube as compared to a flat corona, enhancing face-edge contacts. Thus, switching to PCL creates an emergent lock-and-key binding between cubes and plates through the interplay between the shape of each NC's ligand shell, resulting in the lower well depth. For these reasons, we use PCL as the ligand and select design parameters in stoichiometry and temperature based on the computed phase diagram (Fig. 2B). It is also worth noting that computed PMFs for differently orientated plates lying parallel to the cube's face area are essentially identical to each other, suggesting that in-plane relative orientations of plates are less important compared to the emergent lock-and-key CP interactions. As such, we note that the critical design strategy for co-assembly involves modulating CP interactions such that plates prefer to be sandwiched in between cubes.

## Monte Carlo simulations

To verify the morphology predicted via TPT, we use Monte Carlo simulations of triangular nanoplates and nanocubes using HOOMD-blue (*42*). We select several plate fractions ($\phi_{plate}$ = [0.20,0.40,0.60,

and 0.80]) and inverse temperatures (ε = [6,7,8, and 9]) and perform simulations at statepoints defined by these parameters. Interactions between NCs use the computed PMFs for NCs decorated by PCL. For computational efficiency, we map the PMFs to a square-well potential where the interaction strengths are scaled by the relative well depths of the various interaction types and the surrounding ligand corona determines the interaction ranges (see Methods). We then characterized morphology by using Freud (*43*) to compute the $g(r)$ of the bottom layer of NCs in the simulation box (Fig. 4). The three pure-phase morphologies all have peaks that are indicative of their contribution in the system (occurring at 0.25, 0.65, and 1.1, respectively). These peaks match the approximate well locations for each contact type. We determined the dominant architecture by computing the average peak heights for each of the pure architectures over the last 5M steps of the simulation and scaled their heights by the height of the CP peak to ensure that all comparisons are made from the same frame of reference, as shown in Fig. 5. Phase classification is then performed by selecting the motif with the highest fractional contribution. For example, for $\phi_{plate} = 0.4$ and $\varepsilon = 8$, the dominant motif is CP, and thus, we categorize it as a co-assembled morphology. For systems where two motifs are on par with each other (0.2, 6.0) or (0.8, 9.0), we categorize them as a coexisting system of cube/plate co-assembly along with a pure phase of whichever is the excess NC. Visual inspections of each simulation are additionally performed to confirm phase classification using relative peak intensities. In general, our classification works well for low-temperature (high ε) systems. For high-temperature systems $\varepsilon = 6$, we note that $\phi_{plate} = 0.6$ and 0.8 are both visibly disordered, and thus, we classify them accordingly. For (0.8, 7.0), the system largely separates into a prism and cube layer, and thus, we classify it as phase separated. In the cases of (0.8, 6.0), (0.8., 7.0), and (0.6, 6.0), no long-range assembly occurs and peak contribution is dominated by phase-separated PP interactions. We observe places where co-assembly is the dominant contributor (CP contacts >50% of all contacts) and places where two phases make up comparable percentages of the sum of peak heights. The phase diagram in Fig. 4 demonstrates the results of our $g(r)$ peak comparison, where colored diamonds indicate the co-assembled structure observed in simulation. Overall, these charts allow us to reliably determine the morphology for different combinations of $\phi_{plate}$ and ε and give us confidence that the theory and simulation together can reliably predict the expected experimental phases.

## Interfacial assembly

To best follow the theory laid out above, the size of each NC component was optimized to be complementary to each other, with PbTe cube edge lengths of 19.7 ± 1.1 nm and $LaF_3$ triangular plates with edge lengths of 25.4 ± 2.1 nm and 2 nm thick. The liquid-air interfacial assembly method was used to assemble all films for these studies (*44*). First, for the case of single-component $LaF_3$ films, the orientation of the triangular plates can be effectively controlled by changing the polarity of the subphase, in a similar manner to previous results for other platelet NCs (*14*, *34*). To achieve assembly with a columnar morphology, where the triangular plates are oriented parallel to the surface, a nonpolar subphase is used, such as tetraethylene glycol, as shown in Fig. 6B. With a more polar subphase, such as ethylene glycol, the triangular plates align perpendicular to the surface, as shown in

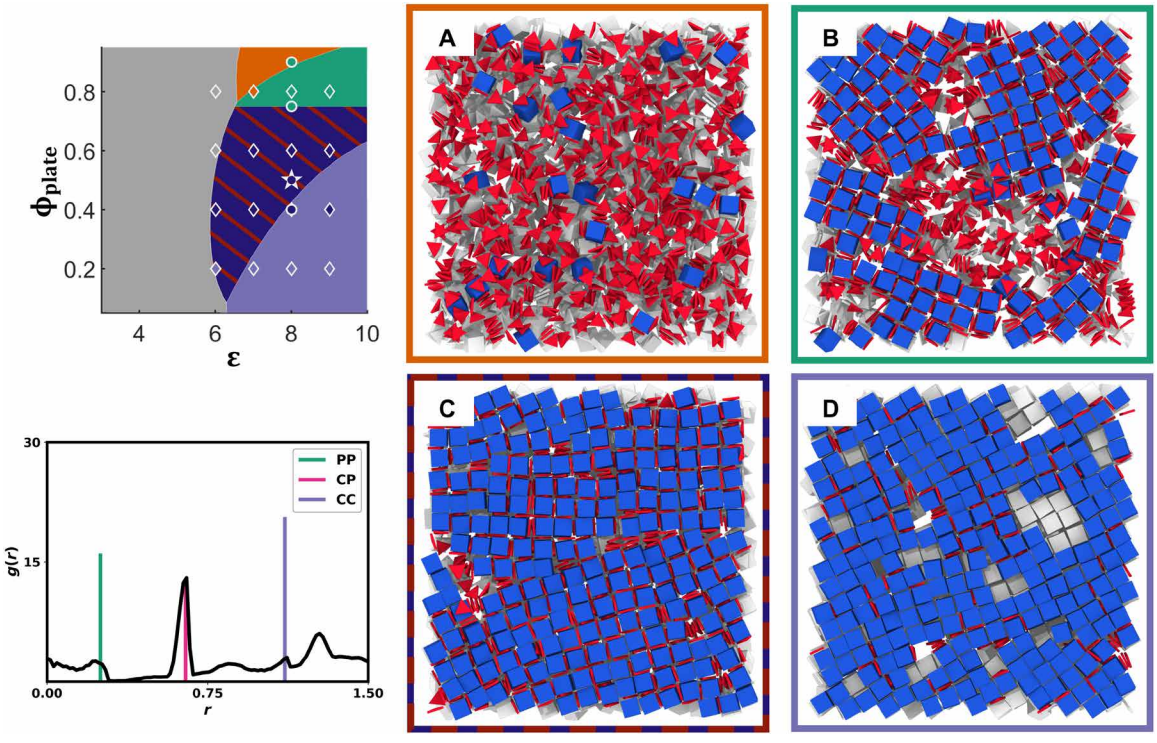


**Fig. 4. Results of Monte Carlo simulations for various ($\phi_{plate}$, ε).** The theoretical phase diagram is overlaid by diamonds representing the matching phase (top left). We include snapshots of the bottom layer of the simulation box (right) representing state points of (0.8, 7.0) (**A**), (0.8, 8.0) (**B**), (0.6, 7.0) (**C**), and (0.2, 8.0) (**D**). Gray NCs indicate NCs not included in the bottom layer. Colored outlines represent the phases that best match the snapshot. We demonstrate that the radial distribution function can identify peaks corresponding to PP, CP, and CC interactions (green, magenta, and purple peaks) [$g(r)$ shown for (0.6, 7.0)].

Fig. 6C. This phenomenon is attributed to repulsive interactions between the surface ligands and the polarity of the subphase. However, after ligand exchange with the bulkier, more hydrophobic PCL, as shown in Fig. 2, the only morphology observed is parallel to the subphase, and multilayer films have an offset architecture, as shown in fig. S1, both of which are consistent with similar studies using this ligand on nanoplates (*34*). Successful ligand exchange is confirmed with both changes in assembly behavior and thermogravimetric analysis (TGA), as shown in fig. S2.

Initial attempts at co-assembly of the OA-coated cubes and triangular plates failed, as anticipated by theory. A few regions with local motifs were observed, which provided evidence that the cubic PbTe could control the orientation of the $LaF_3$. However, for most of the sample, significant aggregation of the PbTe was observed. While these effects were not taken into account when creating the model to guide these experimental efforts, they add to the difficulty of obtaining co-assembly with the limited co-assembly area shown in the phase diagram in Fig. 2.

In switching to the PCL as suggested by theory, successful co-assembly was obtained, as shown in Fig. 7. It highlights that synthesizing NCs with complementary dimensions is not sufficient for successful co-assembly, and optimizing the surface chemistry of each component by tuning of the ligand shell is a critical variable. In this architecture, the PbTe cubes dictate overall film morphology, while $LaF_3$ fills interstitial space in-between the cubes, consistent with the predicted model. Energy-dispersive X-ray spectroscopy (EDS) confirming NC co-assembly is shown in Fig. 7C. Tilt tomography of this co-assembly is included in fig. S4, and high-resolution transmission electron microscopy (TEM) is shown in fig. S5. After examining 450 PbTe cubes, it becomes clear that most of the cubes have at least one triangle assembled on each side. Figure S6 shows how many triangles are present next to each side of the cubes and when there are multiple triangles assembled on the same side of a cube, which are counted separately. When three or four of a cube's sides have triangles assembled on their faces, it is frequently observed that an additional triangle will assemble on at least one of the sides, which is the case 212 times out of 450. For those counted, there were zero observed cubes without at least one triangle assembled next to it. In addition, the superlattice of cubes forms on top of a layer of the triangular plates highlighted in fig. S1, which adds an additional side of the cubes where a triangle is present.

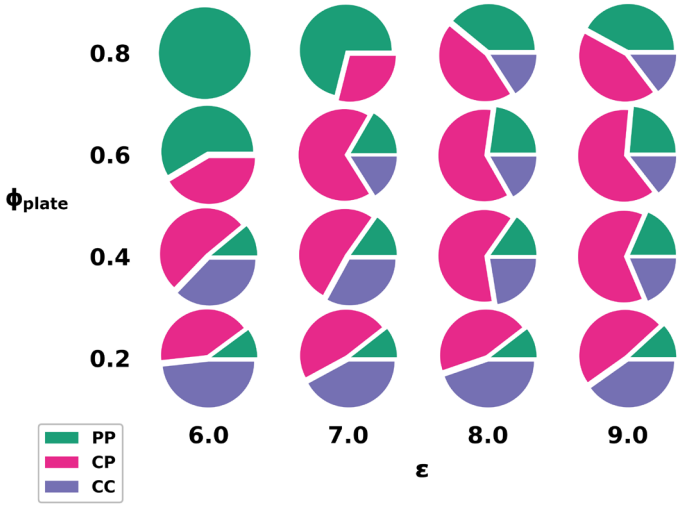


**Fig. 5. Phase classification using relative peak heights.** We demonstrate the various contributions to the final assembly by computing the contribution of contacts (peak height) for PP, CP, and PP, respectively, at various ($\phi_{plate}$, ε). Dominant phases are identified by comparing their relative contributions to the sum of peak heights.

As stated earlier, the PbTe cubes dictate the overall film morphology when concentrations of the cubes are optimized to yield a crystalline superlattice. However, it is also interesting to consider the case when there is a lower concentration of cubes to fully investigate the impact of doping cubes into films that are overwhelmingly composed of triangles and to further test our model. As can be seen in Fig. 8B, in areas of a majority-cube superlattice where a grain boundary is present, or there is a gap between cubes in the film, the triangular plates can form lamellar bridges spanning the distance between the cubes. As the cube concentration decreases, as shown in Fig. 8 (C and D), the cubes still cluster within a film of triangles; however, in these cases, when there is a larger distance between cubes, the triangular plates form lamellar bridges. These bridges can form without two cubes on either end, i.e., when there is only one cube on one side, but these instances are significantly less common. Typically, these lamellar bridges are composed of three or four plates, although longer bridges, for example, 13 plates as in Fig. 8C, are observed as well. In these examples, the cubes still assemble on top of a film of triangular plates, which, due to the PCL on their surfaces, assemble into architectures where one layer of triangular plates is offset from the layer on top of it, consistent with previous results (*34*). The experimental results are compared to the predicted theory by plotting the data points onto the previously shown phase diagram, as shown in Fig. 8. Our theoretical model is in good agreement with the experimental results, particularly for the bullseye case for when the two NCs co-assemble successfully into a uniform lattice.

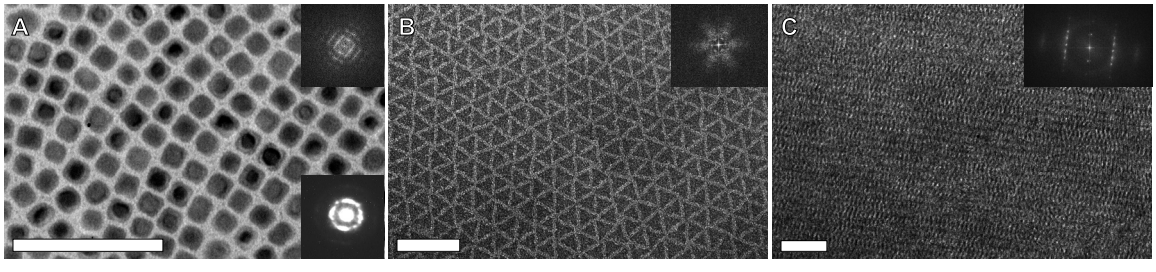


**Fig. 6. Single-component NCs self-assembled with OA as the capping ligand.** TEM images of (**A**) PbTe with selected-area electron diffraction (SAED) inset in the lower right corner, (**B**) $LaF_3$ assembled on tetraethylene glycol, and (**C**) $LaF_3$ assembled on ethylene glycol forming lamella morphology. Scale bars, 100 nm. FFT images are upper right corner insets.

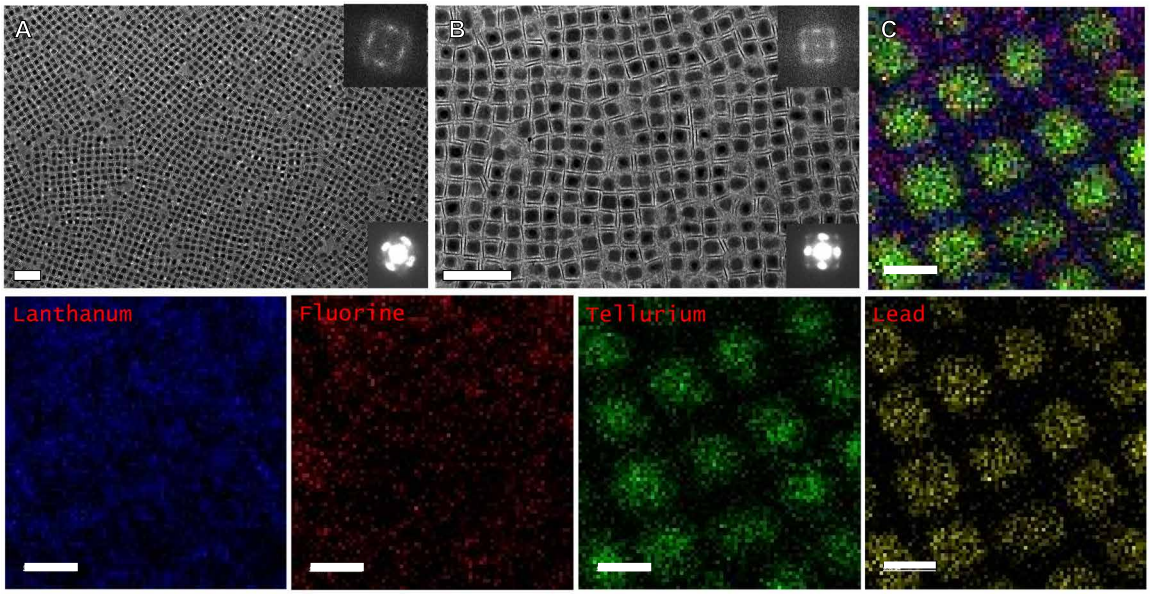


**Fig. 7. Successful co-assembly of PbTe and $LaF_3$.** (**A** and **B**) TEM images at various magnifications. Scale bars, 100 nm (with FFT insets in the upper right corners and small-angle SAED in the lower right corners). (**C**) EDS spectroscopy overlay, with each element listed. Scale bars, 20 nm.

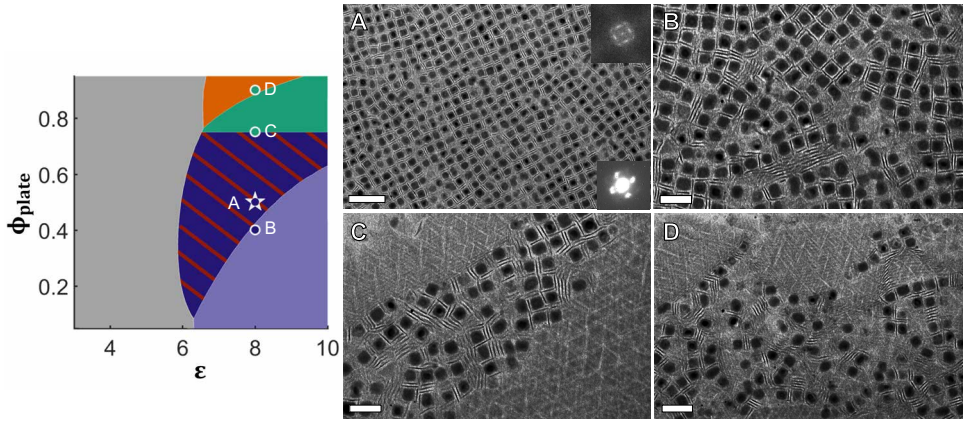


**Fig. 8. Comparison of experiments with the predicted phase diagram.** Corresponding TEM images for a series of points are labeled within the diagram. (**A**) Co-assembly with highest uniformity and a bullseye within the phase diagram, with FFT and small-angle SAED as insets in the upper and lower right corners. Lamellar morphologies in domains with fewer cubes than triangles can be clearly seen in (**B**) to (**D**), which match well with predicted phases. Scale bars, 100 nm (A) and 50 nm (B to D).

Taking our developing design rules for co-assembly of anisotropic NCs and extending them, combinations of two plate NCs of different shapes were explored. This system was selected to probe if the design principles learned in the previous example could be generalized to additional NC choices without additional lattice predictions. In the previous example, assembly of the triangular plates is guided by the cubes due to the strong face-face interactions. The case for two 2D components is unique as the thickness of each edge is only 2 nm, which markedly reduces the area for NC-NC interactions when both plates assemble parallel to the assembly interface. Without a 3D component, neither NC should guide the assembly of the other; rather, this type of co-assembly should be more similar to doping. Nevertheless, successful co-assembly of two anisotropic plate materials has been elusive, as differences in material composition, size, or shape lead to phase segregation.

$GdF_3$:Yb/Er (20/2 mole percent) rhombic plates were chosen to combine with the previous $LaF_3$ triangular plates, as they have complementary shapes. These rhombic plates are 25.4 ± 2.4 nm by 23.6 ± 1.9 nm on their long and short sides, respectively. Similar to the previous study, initial attempts at co-assembly were unsuccessful with the native surface ligand, OA, as the two species phase segregate and exhibit mixed orientations with most subphase choices, highlighted by fig. S7. Excess OA was added to the solutions, as the presence of extra free ligand in NC solutions has aided assembly in previous studies (*45*). However, phase segregation was still the dominant morphology of the obtained films. Following our previous strategy, to align the NCs and enhance co-assembly, the PCL was grafted to the surfaces of both $GdF_3$ and $LaF_3$, resulting in the films shown in Fig. 9 (A and B) and fig. S8. In these films, both components are distributed throughout the assemblies. For the case where there are more $LaF_3$ triangular

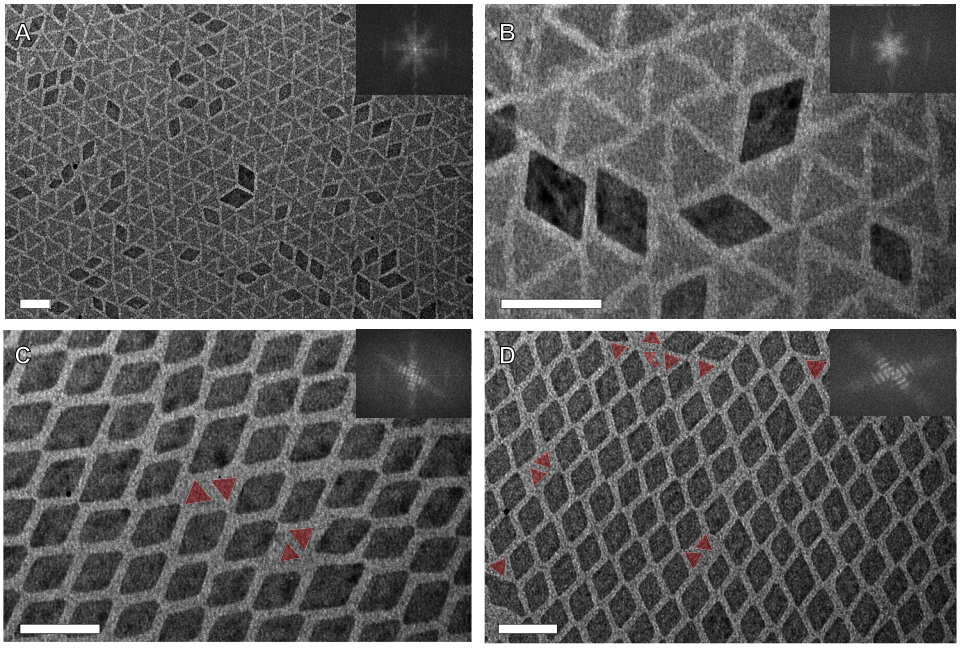


**Fig. 9. Co-assembly of $GdF_3$ rhombic plates with $LaF_3$ triangular plates.** (**A** and **B**) Co-assembly with appropriate edge-length matching, where assembly can be dictated by the concentrations of each component. (**C** and **D**) Smaller triangular plates are used in assembly for substitutional doping into film morphologies of the rhombic plates. FFTs are upper right insets. Scale bars, 50 nm. False coloring has been added to (C) and (D) to highlight the doping.

plates present, the crystallinity of their assembly is undisturbed by the presence of the $GdF_3$ plates. While the PCLs are large enough to shield some of the van der Waals forces between the NCs, clustering of similar NCs is still present in the films. Often groupings of two or three $GdF_3$ plates will assemble in the films, leading us to believe that there are still attractions between NCs of the same composition.

These groupings provide an opportunity for substitutional doping of one larger anisotropic NC for two smaller ones. In Fig. 9 (C and D), we show that the size of the $LaF_3$ triangular plates can be tuned such that two triangular plates better size-match one rhombic plate. These smaller $LaF_3$ triangular plates have edge lengths of 14.9 ± 0.7 nm. Using this strategy, substitutional doping can be achieved for this system, where the film morphology is dictated by the rhombic plates, as highlighted by the fast Fourier transform (FFT) insets. The triangular plates can also fill in void space between grain boundaries within the film, as shown in Fig. 9D and fig. S9. This is the first example of substitutional doping with two anisotropic materials, a key step in advancing assembly choices of nanoscale building blocks. An important finding in this example is that with the appropriate ligand choice, a degree of heterogeneity within the NCs is tolerated during assembly, which is apparent in Fig. 9. This provides greater flexibility to the experimentalist, as control of size distributions in some NC materials still remains a challenge.

## DISCUSSION

In summary, we used a theory- and simulation-driven design approach for the selection of experimental design handles to drive the co-assembly of nanocubes and triangular nanoplates with strong phase segregation tendencies. We show that our theoretically predicted phase diagram can guide computational and experimental selections of parameters across a large phase space to target the co-assembly region of interest. Dissecting the underlying driving forces contributing to co-assembly reveals why the PCL enhances both lattice yield and stability, and extension of this design principle to another system produced a similar success in co-assembly behavior. These results suggest that co-assembly of binary systems can be achieved via the usage of ligands as handles for tuning the relative degree of attraction/repulsion between NCs. Enhancements in attraction are attained through strategically selecting ligand shells, modulating the effective shape of the interacting NCs, and exhibiting emergent lock-and-key interaction motifs that suppress phase segregation. Doing so enables us to tune out geometrical incompatibilities between NCs, shifting otherwise noncomplementary shapes into those that co-assemble through interplays between emergent concave/convex regions within their respective ligand shell. This design strategy opens a potential path forward for the inverse design of the cocrystallization of other binary shape systems, a large step toward precisely engineered metamaterials.

## METHODS

### Thermodynamic perturbation theory

Our TPT calculations start by defining a "hard-particle" reference for cubes and triangular plates arranged in the various co-assembled morphologies of interest. The change in lattice free energy of formation is then computed by first assigning a distribution of interaction sites to all NCs. For any given distribution of surface sites, a PMF can be computed for a pair of NCs across a range of different NC orientations. Briefly, to compute PMF between NCs, we first use our previously developed scaling theory for dendrimeric grafts (*34*) to determine the effective shape of the ligand-grafted NCs. The effective NC shape provides knowledge of where ligands partition on the surfaces of NC, enabling distance-dependent averaging of ligand-ligand interactions between NCs and the quantification of PMFs. We then

combine the PMFs and NC configurations (defined by the hard-particle reference) to compute the equilibrium constant for that lattice of interest as

$$K = \prod_i \sum_j \frac{\rho_j^{s_{ij}}}{s_{ij}!} \int f_{ij}^{s_{ij}}(r)\, g_{ij,c}(r)\, d\vec{r} \quad (1)$$

where the product over $i$ is over the types of interactions in the system, and the summation over $j$ is over all NC types within each interaction type. $f_{ij}(r)$ is the traditional Mayer-$f$ function obtained from a standard cluster expansion and is equivalent to $e^{-\beta V} - 1$, where $V$ is the PMF. The product over interaction types is analogous to the classical thermodynamic limit of defining a net equilibrium constant for a series of reactions as the product of each reaction's individual equilibrium constant, that is, $K_{net} = \prod_i K_i$. ρ is the system density, $g_c(r)$ is the radial distribution function of the reference state, and $s$ is a coordination number defined by the given crystal structure. The prefactor $\left[\frac{\rho_j^{s_{ij}-1}}{s_{ij}}\right]$ accounts for indistinguishability and the probability of finding $s - 1$ NCs that are of interaction type $i$ and species $j$ within the cutoff interaction distance. A full derivation of the theory can be found in the Supplementary Materials of previous works on DNA-mediated self-assembly (*39*, *40*). The lattice free energy of formation $\Delta G$ can then be computed via the standard thermodynamic relation $\Delta G = -kT \ln K_{net}$. It is important to note here that the free energy of lattice formation is determined from a combination of both the NC spatial and orientation ordering, as defined by $g_c(r)$ and PMFs, respectively. In other words, for any given structure, $\Delta G$ is computed using PMFs of different NC orientations and the one that yielded the lowest $\Delta G$ is selected as the equilibrium orientational configuration. All computations are performed for 3D lattices. All our calculations use the approximately similar relative size between plates and cube as were measured in experiments. Specifically, plate thickness is defined to be ~10% of edge length and prism edge length is ~15% larger than edge length of cubes. The parameter defining the ligand uses our previously developed scaling theory (*34*) to encapsulate the effect of ligand architecture into an effective bulkiness parameter $b_{nl}$. $b_{nl} = 1$ and 4 for OA and PCL, respectively.

## Simulation in confinement

Simulations were first attempted via compression of 3D particles into a 2D film. We initialized a small system of 512 particles into a 3D box and then compressed in the $z$ direction until the box thickness reached a value of 1.0, which only allowed for one layer of formation in the system (system packing fraction was constant at 0.40). We performed these simulations for various cube fractions [$\phi_{cube}$ = (0.20,0.40,0.60, and 0.80)] and inverse temperatures [ε = ()] and ultimately found that these simulations could not be representative of the physical behavior observed in experiment. Plates were kinetically restricted from entering the space between cubes due to the thin nature of the simulation box, and cube aggregation was the primary observation. We opted instead for the gravity-driven simulations demonstrated in the main text, which give plates the opportunity to move themselves in the cubic gaps and are free from the kinetic issues observed here.

## Monte Carlo simulation

In each simulation, $N = 1728$ NCs were placed into a 3D box with periodic boundary conditions in only the $x$ and $y$ direction, with $\phi_{plate}$ stoichiometry and inverse temperature of ε. Our Monte Carlo simulations attempt translational and rotational local moves according to the Metropolis criterion, reproducing stochastic Brownian motion of the NCs. Gravitational force was applied in the $z$ direction to pull NCs to the bottom of the simulation box to model self-assembly at the interface. Initially, NCs were simulated for 1M Monte Carlo (MC) moves with $V(r) = 0$ to thermalize the system. Next, NCs were simulated for 20M MC moves using the computed PMFs from theory at inverse temperature ε. We additionally implement small oscillations in inverse temperature about the set point to simulate thermal annealing. This procedure mimics thermal annealing to remove kinetically trapped structures that are initially formed in the simulation.

## Materials

The following materials were used: lead(II) oxide (99.9+%, trace metal basis, <10-μm powder; Acros Organics), tellurium shot (Te, 99.9999%; Alfa Aesar), OA (90%, technical grade; Aldrich Chemistry), 1-octadecene (ODE; 90%, technical grade; Acros Organics), and tributylphosphine (TBP; >93.5%; Sigma-Aldrich). Solvents toluene and isopropyl alcohol were purchased from Thermo Fisher Scientific and used without further purification.

## NC synthesis

### *Synthesis of PbTe cubes*

Synthesis of PbTe cubes was modified from previously reported methods (*46*). PbO (450 mg), octadecene (19 ml), and OA (2.7 ml) were added to a three-neck 50-ml flask. The mixture was degassed under vacuum while stirring at 100°C for 30 min. The mixture changed from orange to clear as the lead and OA underwent complexation. Under nitrogen, the solution was heated to 190°C. TBP-Te was prepared by stirring air-free TBP and tellurium at 50°C in a glovebox for 1 hour. After the temperature stabilized to 190°C, 1.5 ml of air-free 1 M TBP-Te was rapidly injected into the vigorously stirring solution, instantaneously inducing nucleation. The NCs were allowed to grow for 12 min at 190°C, after which the solution was rapidly quenched by injecting 5 ml of toluene. The reaction was further cooled via forced air to about 80°C. The nanocubes were washed and selected for size by adding an equal part of isopropyl alcohol and centrifuging, redispersing in toluene, and repeating twice.

### *Synthesis of $LaF_3$ triangular plates*

Synthesis of $LaF_3$ triangular plates was adapted from previous methods (*35*). La $(CF_3COO)_3$ (0.496 g), OA (6.3 ml), and octadecene (6.5 ml) were added to a tapered three-neck round-bottomed flask. The reaction mixture was stirred vigorously and heated to 100°C for 1 hour under vacuum before heating to 280°C for 1 hour under $N_2$ atm. The solution was then cooled to room temperature followed by addition of ethanol and centrifugation at 8000 rpm for 3 min. The resulting NCs were then redispersed in hexane and precipitated with ethanol and centrifugation twice more to purify the reaction mixture before being suspended in hexane for further use.

### *Synthesis of $GdF_3$ rhombic plates and PCL*

Synthesis of $GdF_3$ rhombic plates and PCL has been described previously (*34*).

### *Ligand exchange with PCL*

A 1-ml solution of OA-capped NCs (10 mg/ml) in hexanes was added to a solution of 10 mg of PCL dissolved in 2 ml of chloroform, and the resulting mixture was stirred at 50°C overnight. The reaction was quenched by addition of ethanol. The resulting precipitate was

collected by centrifugation (6000 rpm, 5 min), and the supernatant liquid was discarded. The solid was redispersed in hexanes under ultrasonic irradiation (2 min) and precipitated by addition of ethanol. This step was repeated at least twice to remove any excess ligands.

### *Self-assembly of NCs*

NC superlattices were obtained using the liquid-air interface assembly method, as described previously (*44*). Selected subphase (1.7 ml) was loaded into a well (1.5 $cm^2$ × 1.0 cm deep machines into Teflon), and a suspension of NCs in hexanes (0.05 mg/ml) was cast onto the surface. This droplet was immediately covered with a glass slide, and the film was left to form over 12 hours. The resulting film was transferred onto TEM grids, and any residual subphase was removed under vacuum before characterization.

### *Characterization*

*Electron microscopy.* TEM micrographs were collected using a JEOL 1400 microscope operated at 120 kV. The TEM was calibrated using a MAG*I*CAL TEM calibration standard. High-resolution STEM micrographs were obtained using a JEOL F200 electron microscope with Cold-FEG emission source operated at 200 kV.

*Thermal analysis.* TGA was carried out using a TA Instruments TGA Q600 apparatus in the temperature range of 25° to 500°C under $N_2$ flow at a heating rate of 10°C/min.

## SUPPLEMENTARY MATERIALS

Supplementary material for this article is available at http://advances.sciencemag.org/cgi/content/full/7/23/eabf9402/DC1

## REFERENCES AND NOTES


1. X. Ye, J. E. Collins, Y. Kang, J. Chen, D. T. N. Chen, A. G. Yodh, C. B. Murray, Morphologically controlled synthesis of colloidal upconversion nanophosphors and their shape-directed self-assembly. *Proc. Natl. Acad. Sci. U.S.A.* **107**, 22430–22435 (2010).
2. T. Huang, Q. Zhao, J. Xiao, L. Qi, Controllable self-assembly of PbS nanostars into ordered structures: Close-packed arrays and patterned arrays. *ACS Nano* **4**, 4707–4716 (2010).
3. Y. Liu, K. Deng, J. Yang, X. Wu, X. Fan, M. Tang, Z. Quan, Shape-directed self-assembly of nanodumbbells into superstructure polymorphs. *Chem. Sci.* **11**, 4065–4073 (2020).
4. Q. Wang, Z. Wang, Z. Li, J. Xiao, H. Shan, Z. Fang, L. Qi, Controlled growth and shape-directed self-assembly of gold nanoarrows. *Sci. Adv.* **3**, e1701183 (2017).
5. M. Jiang, X. Peng, Anisotropic $Fe_3O_4$/$Mn_3O_4$ hybrid nanocrystals with unique magnetic properties. *Nano Lett.* **17**, 3570–3575 (2017).
6. Z. Quan, H. Xu, C. Wang, X. Wen, Y. Wang, J. Zhu, R. Li, C. J. Sheehan, Z. Wang, D.-M. Smilgies, Z. Luo, J. Fang, Solvent-mediated self-assembly of nanocube superlattices. *J. Am. Chem. Soc.* **136**, 1352–1359 (2014).
7. J. Henzie, M. Grünwald, A. Widmer-Cooper, P. L. Geissler, P. Yang, Self-assembly of uniform polyhedral silver nanocrystals into densest packings and exotic superlattices. *Nat. Mater.* **11**, 131–137 (2012).
8. Y. Nagaoka, R. Tan, R. Li, H. Zhu, D. Eggert, Y. A. Wu, Y. Liu, Z. Wang, O. Chen, Superstructures generated from truncated tetrahedral quantum dots. *Nature* **561**, 378–382 (2018).
9. X. Ye, J. Chen, M. Engel, J. A. Millan, W. Li, L. Qi, G. Xing, J. E. Collins, C. R. Kagan, J. Li, S. C. Glotzer, C. B. Murray, Competition of shape and interaction patchiness for self-assembling nanoplates. *Nat. Chem.* **5**, 466–473 (2013).
10. M. P. Arciniegas, M. R. Kim, J. De Graaf, R. Brescia, S. Marras, K. Miszta, M. Dijkstra, R. van Roij, L. Manna, Self-assembly of octapod-shaped colloidal nanocrystals into a hexagonal ballerina network embedded in a thin polymer film. *Nano Lett.* **14**, 1056–1063 (2014).
11. K. Miszta, J. de Graaf, G. Bertoni, D. Dorfs, R. Brescia, S. Marras, L. Ceseracciu, R. Cingolani, R. van Roij, M. Dijkstra, L. Manna, Hierarchical self-assembly of suspended branched colloidal nanocrystals into superlattice structures. *Nat. Mater.* **10**, 872–876 (2011).
12. Y. Yu, X. Lu, A. Guillaussier, V. R. Voggu, W. Pineros, M. de la Mata, J. Arbiol, D.-M. Smilgies, T. M. Truskett, B. A. Korgel, Orientationally ordered silicon nanocrystal cuboctahedra in superlattices. *Nano Lett.* **16**, 7814–7821 (2016).
13. Y. Gao, M. C. Weidman, W. A. Tisdale, CdSe nanoplatelet films with controlled orientation of their transition dipole moment. *Nano Lett.* **17**, 3837–3843 (2017).
14. T. Paik, D.-K. Ko, T. R. Gordon, V. Doan-Nguyen, C. B. Murray, Studies of liquid crystalline self-assembly of $GdF_3$ nanoplates by in-plane, out-of-plane SAXS. *ACS Nano* **5**, 8322–8330 (2011).
15. R. Momper, H. Zhang, S. Chen, H. Halim, E. Johannes, S. Yordanov, D. Braga, B. Blülle, D. Doblas, T. Kraus, M. Bonn, H. I. Wang, A. Riedinger, Kinetic control over self-assembly of semiconductor nanoplatelets. *Nano Lett.* **20**, 4102–4110 (2020).
16. Z. Ou, Z. Wang, B. Luo, E. Luijten, Q. Chen, Kinetic pathways of crystallization at the nanoscale. *Nat. Mater.* **19**, 450–455 (2020).
17. A. Travesset, Topological structure prediction in binary nanoparticle superlattices. *Soft Matter* **13**, 147–157 (2017).
18. E. V. Shevchenko, D. V. Talapin, N. A. Kotov, S. O'Brien, C. B. Murray, Structural diversity in binary nanoparticle superlattices. *Nature* **439**, 55–59 (2006).
19. E. V. Shevchenko, D. V. Talapin, C. B. Murray, S. O'Brien, Structural characterization of self-assembled multifunctional binary nanoparticle superlattices. *J. Am. Chem. Soc.* **128**, 3620–3637 (2006).
20. Z. Chen, S. O'Brien, Structure direction of II–VI semiconductor quantum dot binary nanoparticle superlattices by tuning radius ratio. *ACS Nano* **2**, 1219–1229 (2008).
21. T. Paik, C. B. Murray, Shape-directed binary assembly of anisotropic nanoplates: A nanocrystal puzzle with shape-complementary building blocks. *Nano Lett.* **13**, 2952–2956 (2013).
22. A. Castelli, J. de Graaf, M. Prato, L. Manna, M. P. Arciniegas, Tic-Tac-Toe binary lattices from the interfacial self-assembly of branched and spherical nanocrystals. *ACS Nano* **10**, 4345–4353 (2016).
23. X. Ye, J. A. Millan, M. Engel, J. Chen, B. T. Diroll, S. C. Glotzer, C. B. Murray, Shape alloys of nanorods and nanospheres from self-assembly. *Nano Lett.* **13**, 4980–4988 (2013).
24. T. Paik, B. T. Diroll, C. R. Kagan, C. B. Murray, Binary and ternary superlattices self-assembled from colloidal nanodisks and nanorods. *J. Am. Chem. Soc.* **137**, 6662–6669 (2015).
25. J. Hao, Y. Yang, F. Zhang, Z. Yang, J. Wei, Faceted colloidal Au/$Fe_3O_4$ binary supracrystals dictated by intrinsic lattice structures and their collective optical properties. *J. Phys. Chem. C* **124**, 14775–14786 (2020).
26. Y. Yang, B. Wang, X. Shen, L. Yao, L. Wang, X. Chen, S. Xie, T. Li, J. Hu, D. Yang, A. Dong, Scalable assembly of crystalline binary nanocrystal superparticles and their enhanced magnetic and electrochemical properties. *J. Am. Chem. Soc.* **140**, 15038–15047 (2018).
27. Y. Wu, S. Li, N. Gogotsi, T. Zhao, B. Fleury, C. R. Kagan, C. B. Murray, J. B. Baxter, Directional carrier transfer in strongly coupled binary nanocrystal superlattice films formed by assembly and in situ ligand exchange at a liquid–air interface. *J. Phys. Chem. C* **121**, 4146–4157 (2017).
28. M. B. Zanjani, J. R. Lukes, Shape- and structure-based phonon bandgap tuning with nanocrystal superlattices. *J. Phys. Chem. C* **119**, 16889–16896 (2015).
29. D. Mendez-Gonzalez, S. Melle, O. G. Calderón, M. Laurenti, E. Cabrera-Granado, A. Egatz-Gómez, E. López-Cabarcos, J. Rubio-Retama, E. Díaz, Control of upconversion luminescence by gold nanoparticle size: From quenching to enhancement. *Nanoscale* **11**, 13832–13844 (2019).
30. W.-L. Ong, E. S. O'Brien, P. S. M. Dougherty, D. W. Paley, C. Fred Higgs III, A. J. H. McGaughey, J. A. Malen, X. Roy, Orientational order controls crystalline and amorphous thermal transport in superatomic crystals. *Nat. Mater.* **16**, 83–88 (2017).
31. E. A. Doud, A. Voevodin, T. J. Hochuli, A. M. Champsaur, C. Nuckolls, X. Roy, Superatoms in materials science. *Nat. Rev. Mater.* **5**, 371–387 (2020).
32. M. Cargnello, A. C. Johnston-Peck, B. T. Diroll, E. Wong, B. Datta, D. Damodhar, V. V. T. Doan-Nguyen, A. A. Herzing, C. R. Kagan, C. B. Murray, Substitutional doping in nanocrystal superlattices. *Nature* **524**, 450–453 (2015).
33. D. Jishkariani, K. C. Elbert, Y. Wu, J. D. Lee, M. Hermes, D. Wang, A. Van Blaaderen, C. B. Murray, Nanocrystal core size and shape substitutional doping and underlying crystalline order in nanocrystal superlattices. *ACS Nano* **13**, 5712–5719 (2019).
34. K. C. Elbert, T. Vo, N. M. Krook, W. Zygmunt, J. Park, K. G. Yager, R. J. Composto, S. C. Glotzer, C. B. Murray, Dendrimer ligand directed nanoplate assembly. *ACS Nano* **13**, 14241–14251 (2019).
35. Y.-W. Zhang, X. Sun, R. Si, L.-P. You, C.-H. Yan, Single-crystalline and monodisperse $LaF_3$ triangular nanoplates from a single-source precursor. *J. Am. Chem. Soc.* **127**, 3260–3261 (2005).
36. T. Lewi, H. A. Evans, N. A. Butakov, J. A. Schuller, Ultrawide thermo-optic tuning of PbTe meta-atoms. *Nano Lett.* **17**, 3940–3945 (2017).
37. S. N. Girard, J. He, X. Zhou, D. Shoemaker, C. M. Jaworski, C. Uher, V. P. Dravid, J. P. Heremans, M. G. Kanatzidis, High performance Na-doped PbTe–PbS thermoelectric materials: Electronic density of states modification and shape-controlled nanostructures. *J. Am. Chem. Soc.* **133**, 16588–16597 (2011).
38. D. Wang, M. Hermes, R. Kotni, Y. Wu, N. Tasios, Y. Liu, B. de Nijs, E. B. van der Wee, C. B. Murray, M. Dijkstra, A. van Blaaderen, Interplay between spherical confinement and particle shape on the self-assembly of rounded cubes. *Nat. Commun.* **9**, 2228 (2018).

39. F. Lu, T. Vo, Y. Zhang, A. Frenkel, K. G. Yager, S. Kumar, O. Gang, Unusual packing of soft-shelled nanocubes. *Sci. Adv.* **5**, eaaw2399 (2019).
40. Y. Tian, J. R. Lhermitte, L. Bai, T. Vo, H. L. Xin, H. Li, R. Li, M. Fukuto, K. G. Yager, J. S. Kahn, Y. Xiong, B. Minevich, S. K. Kumar, O. Gang, Ordered three-dimensional nanomaterials using DNA-prescribed and valence-controlled material voxels. *Nat. Mater.* **19**, 789–796 (2020).
41. K. C. Elbert, J. D. Lee, Y. Wu, C. B. Murray, Improved chemical and colloidal stability of gold nanoparticles through dendron capping. *Langmuir* **34**, 13333–13338 (2018).
42. J. A. Anderson, J. Glaser, S. C. Glotzer, HOOMD-blue: A Python package for high-performance molecular dynamics and hard particle Monte Carlo simulations. *Comput. Mater. Sci.* **173**, 109363 (2020).
43. V. Ramasubramani, B. D. Dice, E. S. Harper, M. P. Spellings, J. A. Anderson, S. C. Glotzer, Freud: A software suite for high throughput analysis of particle simulation data. *Comput. Phys. Commun.* **254**, 107275 (2020).
44. A. Dong, J. Chen, P. M. Vora, J. M. Kikkawa, C. B. Murray, Binary nanocrystal superlattice membranes self-assembled at the liquid–air interface. *Nature* **466**, 474–477 (2010).
45. S. W. Winslow, J. W. Swan, W. A. Tisdale, The importance of unbound ligand in nanocrystal superlattice formation. *J. Am. Chem. Soc.* **142**, 9675–9685 (2020).
46. J. E. Murphy, M. C. Beard, A. G. Norman, S. P. Ahrenkiel, J. C. Johnson, P. Yu, O. I. Mićić, R. J. Ellingson, A. J. Nozik, PbTe colloidal nanocrystals: Synthesis, characterization, and multiple exciton generation. *J. Am. Chem. Soc.* **128**, 3241–3247 (2006).



**Acknowledgments**

**Funding:** We acknowledge support from the Office of Naval Research Multidisciplinary University Research Initiative Award ONR N00014-18-1-2497. K.C.E. acknowledges support from the NSF Graduate Research Fellowship Program under Grant No. DGE-1321851. W.Z. was supported by a National Defense Science and Engineering Graduate (NDSEG) Fellowship, 32 CFR 168a, awarded by the Department of Defense, Air Force Office of Scientific Research under Contract No. FA9550-11-C-0028. D.J.R. acknowledges support from the Vagelos Institute for Energy Science and Technology Fellowship Program. N.M.K. acknowledges the MRSEC-DMR-1720530 program. C.B.M. acknowledges the Richard Perry University Professorship at the University of Pennsylvania. This research was supported, in part, through computational resources and services supported by Advanced Research Computing at the University of Michigan, Ann Arbor. **Author contributions:** K.C.E. synthesized $LaF_3$ NCs and ligands and performed self-assembly and characterization. W.Z. and T.V. performed theory and simulations. C.M.V. synthesized PbTe cubes and N.M.K. synthesized $GdF_3$ rhombic plates. D.J.R. took HRTEMs. K.C.E., W.Z., T.V., S.C.G., and C.B.M. conceived experiments and co-wrote the manuscript with contributions from all the authors. **Competing interests:** The authors declare that they have no competing interests. **Data and materials availability:** All data needed to evaluate the conclusions in the paper are present in the paper and/or the Supplementary Materials. Additional data related to this paper may be requested from the authors.

Submitted 30 November 2020
Accepted 19 April 2021
Published 4 June 2021
10.1126/sciadv.abf9402

**Citation:** K. C. Elbert, W. Zygmunt, T. Vo, C. M. Vara, D. J. Rosen, N. M. Krook, S. C. Glotzer, C. B. Murray, Anisotropic nanocrystal shape and ligand design for co-assembly. *Sci. Adv.* **7**, eabf9402 (2021).